Weighted-average time-lapse seismic full-waveform inversion

Amir Mardan[1], Bernard Giroux[1], and Gabriel Fabien-Ouellet[2]

ABSTRACT

As seismic data can contain information over a large spatial area and are sensitive to changes in the properties of the subsurface, seismic imaging has become the standard geophysical monitoring method for many applications such as carbon capture and storage and reservoir monitoring. The availability of practical tools such as full-waveform inversion (FWI) makes time-lapse seismic FWI a promising method for monitoring subsurface changes. However, FWI is a highly ill-posed problem that can generate artifacts. Because the changes in the earth's properties are typically small in terms of magnitude and spatial extent, discriminating the true time-lapse signature from noise can be challenging. Different strategies have been proposed to address these difficulties. In this study, we propose a weighted-average (WA) inversion to better control the effects of artifacts and differentiate them from the true 4D changes. We further compare five related strategies with synthetic tests on clean and noisy data. The effects of seawater velocity variation on different strategies also are studied as one of the main sources of nonrepeatability. We tested different strategies of time-lapse FWI (TL-FWI) using the Marmousi and the SEG Advanced Modeling time-lapse models. The results indicate that the WA method can provide the best compromise between accuracy and computation time. This method also provides a range of possible answers of other TL-FWI strategies.

INTRODUCTION

Monitoring the earth's properties is an important problem that lead to a better understanding of the processes under the surface. Having a good knowledge of changes in these properties can improve the efficiency of operations either in petroleum production or CO_2 sequestration. An image of these changes can be obtained us-

ing time-lapse geophysical data. This concept can be used with any geophysical method, provided that changes occurring in the underground affect the properties probed with the chosen geophysical method. Alongside the studies on the functionality of time-lapse analysis using nonseismic methods (Davis et al., 2008; Hayley et al., 2011; Giertzuch et al., 2020), interesting research on time-lapse seismic data has been carried out since the 1990s (Lumley, 1995a, 1995b; Altan, 1997; Biondi et al., 1998).

Due to the ability of full-waveform inversion (FWI) to obtain high-resolution images of the subsurface (Tarantola, 1984; Pratt and Worthington, 1990), using this technique in a time-lapse manner is an area of ongoing research. Many studies in recent years focused on making 4D FWI practical and on improving its accuracy and reliability. For example, Watanabe et al. (2005) use time-lapse crosswell seismic data at the Mallik test site during a gas production test from a gas hydrate layer. Routh and Anno (2008) analyze the efficiency of obtaining 4D changes through inverting data difference and model subtraction by studying marine data. Raknes et al. (2013) apply time-lapse FWI (TL-FWI) on marine data acquired in a field in the North Sea to detect the leakage in one of the wells from 1988 to 1990. Maharramov et al. (2016) use TL-FWI to study the effects of oil production on P-wave velocity in the Genesis field in southwest New Orleans between 1999 and 2002. Hicks et al. (2016) use 4D FWI to study the Grane PRM system located in the North Sea to recover the P-wave velocity changes related to the gas replacing oil. Fabien-Ouellet et al. (2017b) appraise the performance of 4D FWI to estimate velocity and attenuation changes for monitoring CO_2 sequestration.

In addition to the research on the feasibility and efficiency of TL-FWI, several studies have been performed to enhance the result and improve the robustness of this technique. This improvement can be obtained through two main strategies: either decreasing the artifacts in the final time-lapse image by estimating multiple models in a way that artifacts cancel out with subtraction of monitor and baseline models or reducing the propagation of the artifacts of the inversion of one vintage to the inversion of the other vintage by implementing simultaneous inversion (SI) (Maharramov and Biondi, 2014).

The most straightforward strategy for TL-FWI is parallel inversion, in which the inversion of the baseline and monitor vintages is performed independently and the results are subtracted. Although this strategy does not yield the most accurate result (Zhou and Lumley, 2021b), it is the basic method for time-lapse inversion and it has been used in different studies as a reference (Watanabe et al., 2005; Plessix et al., 2010; Maharramov et al., 2016). Watanabe et al. (2005) apply the double-difference method developed for time-lapse resistivity tomography to seismic studies. The main disadvantage of this method is its high sensitivity to source/receiver positioning errors (Zhou and Lumley, 2021b). Another scheme is cascaded inversion (Routh et al., 2012). In this method, the inversion of the baseline is used as the initial model for the inversion of the monitor model and finally, the models are subtracted. The drawback of this method is that the generated artifacts in the baseline and monitor estimates are not likely to cancel out. Maharramov and Biondi (2014) present a sequential-difference (cross-updating [CU]) method that needs applying FWI four times. In this method, they first implement the cascaded algorithm during which one baseline and one monitor model are obtained. Then, the inversion schemes continue to obtain another baseline model by using the first estimated monitor model as the initial guess. Finally, the second estimated baseline model is used as the initial model for estimating the monitor model for the second time. The final output of this algorithm is the difference between the second estimations of baseline and monitor models. Zhou and Lumley (2021a) propose the central-difference (CD) strategy that uses two independent cascaded inversions to obtain two bootstraps. Eventually, the average of the two bootstraps gives an accurate estimation of the changes.

The reason Maharramov and Biondi (2014) and Zhou and Lumley (2021a) propose the CU and CD methods is to reduce the bias in the output of the cascaded inversion. Cascaded inversion cannot estimate the changes very well because of the difference in the level of convergence of baseline and monitor models (Hicks et al., 2016). In other words, because FWI is highly sensitive to the initial model, it cannot update the baseline model from the initial guess and update the monitor model from the estimated baseline. This problem is dealt with at the cost of performing the FWI four times (Maharramov and Biondi, 2014; Zhou and Lumley, 2021a). Finally, SI (Maharramov and Biondi, 2014) is another effective strategy for estimating the 4D changes that are fast and accurate. In this method, the two vintages are jointly inverted by using the appropriate regularization terms on the model changes in time. However, the choice of an appropriate regularization parameter can be tedious.

The purpose of this paper is twofold. First, we present a new strategy for TL-FWI aimed to improve the accuracy and decrease the computation time over existing approaches. Second, a comparison of common strategies of 4D FWI is made. In the first part of this study, TL-FWI strategies are discussed and a new method is proposed. This method, called weighted-average (WA) TL-FWI, provides highly accurate results in comparison with other mentioned strategies with less computation time. In the second part, the methods are evaluated using the Marmousi and the SEG Advanced Modeling (SEAM) time-lapse models.

TIME-LAPSE FWI STRATEGIES

FWI is a high-resolution seismic-imaging technique that uses the entire content of seismic traces for extracting the physical parameters of the medium sampled by seismic waves (Virieux et al.,

2017). By recasting the migration imaging principle, Tarantola (1984) proposes FWI as a local optimization problem that tries to minimize the least-squares misfit between the recorded and modeled data. This problem can be formulated as

$$\min_{\mathbf{m}} \mathcal{C}(\mathbf{m}) = \frac{1}{2} \|F(\mathbf{m}) - \mathbf{d}\|_2^2, \tag{1}$$

where F and $\mathbf{m}$ are, respectively, the forward-modeling operator and model parameters and $\mathbf{d}$ is the observed data. To minimize the cost function, the solutions are computed by updating the model vector $\mathbf{m}$ with a descent direction $\Delta\mathbf{m}$:

$$\mathbf{m}^{k+1} = \mathbf{m}^k + \alpha^k \Delta\mathbf{m}^k, \tag{2}$$

where superscript k denotes the iteration number and α is the step size which is estimated using the line search method (Nocedal and Wright, 2006). To solve this problem, numerous methods can be deployed such as the conjugate-gradient method, the limited-memory Broyden–Fletcher–Goldfarb–Shanno (l-BFGS) approach, Gauss-Newton, and truncated Newton methods (Virieux and Operto, 2009). Note that, in this study, the l-BFGS method is used which partially uses the Hessian matrix (Nocedal and Wright, 2006). The minimization of this problem is done in the vicinity of an initial model $\mathbf{m}^0$ (Virieux and Operto, 2009). As FWI is a highly ill-posed problem, this initial guess affects the output of the algorithm significantly, i.e., different initial models can lead to different estimations. Therefore, the main goal of the time-lapse strategies is to efficiently decrease the effects of initial guesses on the estimated time-lapse image. As this paper focuses on time-lapse methods, the interested readers are referred to the comprehensive review of Virieux and Operto (2009) for further details on FWI.

In what follows, we review different strategies for TL-FWI. These methods include the cascaded (CC), CU, CD, WA, and SI inversions. The computation time of each method is expressed in terms of the number of required FWI runs as well as the relative cost with respect to the cascaded method which is the fastest approach. It should be noticed that for SI, the procedure yields two models (baseline and monitor models), and its computational cost is approximately twice that of a single FWI run.

Cascaded inversion

The cascaded TL-FWI strategy consists of inverting first the baseline data and then using the estimated model as the starting model $\mathbf{m}^0 = \mathbf{m}_b$ for the monitor data (Routh et al., 2012). The monitor model is estimated as

$$\mathbf{m}_m = \mathbf{m}_b + \sum_{k=1}^{N_{\text{iter}}} \alpha^k \Delta\mathbf{m}^k, \tag{3}$$

where N_{iter} is the number of iterations. As shown in Figure 1a, the final estimation of parameter changes is obtained by subtracting the baseline from the monitor model. This method tends to introduce large artifacts in the time-lapse estimate. However, if we first estimate the monitor model and use it as the initial model to obtain the baseline model, the estimated time-lapse image changes although it should not.

In terms of computation time, this method needs two FWI runs: one run on the baseline data and another run on the monitor data to estimate the corresponding model using the estimated baseline model.

CU inversion

To reduce the flaws of the cascaded method, Maharramov and Biondi (2014) propose the CU technique, which also is called sequential or double-cascaded inversion in the literature (Hicks et al., 2016). In this method, the time-lapse inversion is undertaken as two consecutive cascaded inversions. The flowchart of this approach is shown in Figure 1b. First, the cascaded method is performed to estimate an image of baseline ($\mathbf{m}_b$) followed by a monitor model ($\mathbf{m}_m$). Then, the algorithm uses the estimated monitor model as the initial guess ($\mathbf{m}^0 = \mathbf{m}_m$) for another cascaded inversion to estimate the second set of baseline and monitor models as $\mathbf{m}_b'$ and $\mathbf{m}_m'$. Finally, the 4D model is calculated as

$$\Delta\mathbf{m} = \mathbf{m}_m' - \mathbf{m}_b'. \tag{4}$$

The CU method needs four FWI runs (two on the baseline data and two on the monitor data).

The CD method

An alternative strategy to deal with the artifacts caused by the starting model is the CD method (Zhou and Lumley, 2021a). In this strategy, two cascaded inversions are performed independently with the same initial guess (Figure 1c). The first inversion consists of inverting the baseline data and using the estimated model ($\mathbf{m}_b$) as the initial model for inverting the monitor data (the same as the cascaded inversion). The output of this time-lapse inversion is called the forward bootstrap. For the reverse bootstrap, the monitor data are first inverted to estimate a monitor model ($\mathbf{m}_m$) and then this monitor model is used as the initial model to obtain another estimate of the baseline model ($\mathbf{m}_b'$). Although performing this strategy provides four approximations of 4D changes, the average of two bootstraps yields the most accurate estimate (Zhou and Lumley, 2021a). Based on the four possible estimates of the 4D changes, Zhou and Lumley (2021a) introduce the reverse and forward bootstraps as, respectively,

$$\Delta\mathbf{m}^- = \mathbf{m}_m - \mathbf{m}_b', \tag{5a}$$

$$\Delta\mathbf{m}^+ = \mathbf{m}_m' - \mathbf{m}_b. \tag{5b}$$

As shown in the study of Zhou and Lumley (2021a), reverse and forward bootstraps have different signs at the location of most of the artifacts, whereas the opposite is true for the sought anomalies. Based on this fact and inspired by the finite-difference method, Zhou and Lumley (2021a) propose to estimate the 4D changes as the average of two bootstraps:

$$\Delta\mathbf{m} = \frac{\Delta\mathbf{m}^- + \Delta\mathbf{m}^+}{2}. \tag{6}$$

Similar to the CU method, this strategy needs four FWI runs.

The WA method

Although the CU and CD methods allow generating a good estimate of time-lapse changes in

the properties of the subsurface, they need four FWI runs and are therefore time consuming. To decrease the computation time, we propose a new version of the cascaded-base strategy. In this method, which we call WA TL-FWI, we need to run FWI three times (Figure 1d).

In WA TL-FWI, the reverse and forward bootstraps are redefined as

$$\Delta\mathbf{m}^- = \mathbf{m}_m - \mathbf{m}_b, \tag{7a}$$

$$\Delta\mathbf{m}^+ = \mathbf{m}_m - \mathbf{m}_b'. \tag{7b}$$

Contrary to the CD method, the WA method estimates only one monitor model (no need to estimate $\mathbf{m}_m'$). To avoid confusion with equation 5, it should be mentioned that the terms of reverse and forward bootstraps hereafter indicate the estimated changes obtained in equation 7 (the WA method).

Zhou and Lumley (2021a) assert that the existing artifacts on the reverse bootstrap appear on the forward bootstraps with a phase reversal. However, the true changes in the model are estimated with the same sign in both bootstraps. The artifacts on the reverse and forward bootstraps cancel out each other, whereas the true changes in the model add up when summing the bootstraps. However, artifacts do not always cancel out perfectly in practice. To account for this fact, we propose a weighted average of the bootstraps:

$$\Delta\mathbf{m} = \frac{\beta\Delta\mathbf{m}^- + \Delta\mathbf{m}^+}{1 + \beta}. \tag{8}$$

Parameter β mostly affects the artifacts and makes them more or less noticeable. Hence, changing this parameter and comparing the results is a good way to detect the true anomalies. By changing this parameter, we can easily see how the artifacts cancel out and disappear, whereas the true anomalies change only slightly in their value. As will be shown later, a good estimation of β can be obtained by plotting the ℓ_1-norm of the estimated image for different values of β.
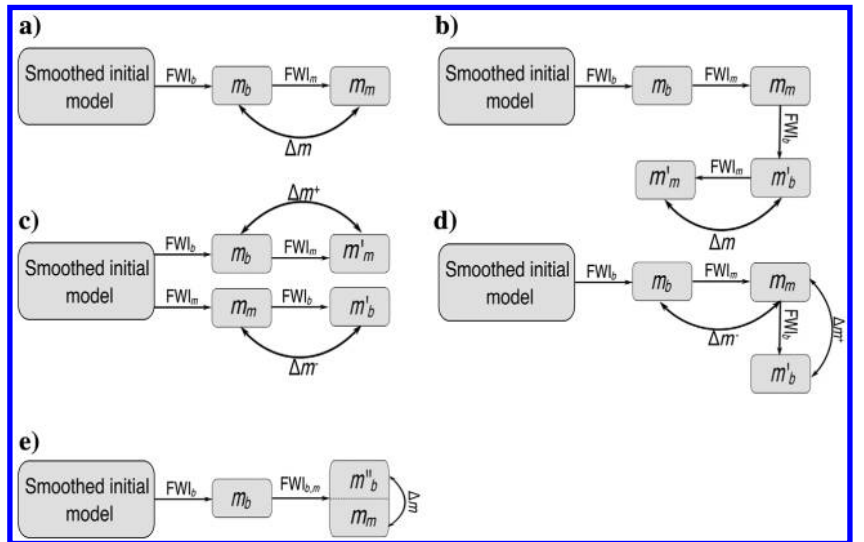

Figure 1. Flowcharts of different TL-FWI strategies. (a) CC, (b) CU, (c) CD, (d) WA, and (e) SI methods.

The SI method

An alternative to implementing FWI individually for each vintage is the joint inversion of the baseline and monitor model. Maharramov and Biondi (2014) propose this method by introducing the cost function of the time-lapse problem as

$$\min_{\mathbf{m}_m, \mathbf{m}_b} \mathcal{C}(\mathbf{m}_m, \mathbf{m}_b) = \|F(\mathbf{m}_b) - \mathbf{d}_b\|_2^2 + \|F(\mathbf{m}_m) - \mathbf{d}_m\|_2^2$$
$$+ \delta \|\mathbf{m}_m - \mathbf{m}_b\|_2^2, \qquad (9)$$

where δ is the regularization factor. The algorithm is shown in Figure 1e. In this strategy, FWI is applied to the baseline data to estimate the baseline model from a smoothed initial model. In the next step, this model is used as the initial model for the joint inversion of the baseline and monitor data. As shown in Figure 1e, this method needs two FWI steps in which three models (one monitor and two baseline models) are estimated.

CASE STUDY

In this section, we analyze the efficiency of the time-lapse inversion strategies using the Marmousi model which has been used previously for testing time-lapse imaging algorithms (Maharramov and Biondi, 2014; Asnaashari et al., 2015; Yang et al., 2016; Li et al., 2021). Following this first series of tests, the WA inversion is used to estimate a time-lapse image of the SEAM model. Note that the density is considered constant during the computations. This assessment is carried out in the case of noise-free and noisy data.

The Marmousi experiment

In the first part of this case study, the Marmousi model is used. In addition to the perfectly repeated acquisition of the monitor model, we analyze the efficiency of different TL-FWI methods in the presence of a nonrepeatability (NR) issue. Studies have shown that an effective inversion strategy can reduce the effects of NR on time-lapse estimates (Kamei and Lumley, 2017; Zhou and Lumley, 2021b). In this study, the NR is modeled by considering a warm sublayer of seawater with a horizontal gradient in V_P linearly increasing from 0.3% to 2% of the water velocity (1500m/s) at the top of the monitor model (Zhou and Lumley, 2021b). This model of NR is chosen as Zhou and Lumley (2021b) study the effects of different sources of NR such as source-receivers positioning errors, coordinate measurement errors, tidal water level variation, and seawater velocity variation errors, and they show that seawater velocity variation can cause significant artifacts in the time-lapse estimate which also is difficult to deal with during the processing.

The baseline velocity model for the Marmousi model was created by filling the gas reservoirs in this model with the velocity of the background (Figure 2a). The monitor velocity models are shown in Figure 2b and 2c without and with NR, respectively. Figure 2d shows the smoothed initial model used to perform this study. Note that the color scale is particularly chosen in Figure 2a–2d for better visualization of the shallow warm water (NR). Figure 2e shows the time-lapse changes between the baseline and perfectly repeated monitor model in the absolute value of percent changes. The highest velocity variation in this model with respect to the baseline is 23%. This is consistent with studies such as Fabien-Ouellet et al. (2017b) and Zhou and Lumley (2021a, 2021b). The true time-lapse image with NR is shown in Figure 2f.

For this study, a surface acquisition is carried out. The acquisition geometry contains 10 isotropic explosive sources with 223 receivers spaced every 7 m. The source is a Ricker wavelet with a central frequency of 15 Hz. The data are modeled using acoustic finite-difference modeling in the time domain by taking advantage of the leap-frog strategy (Virieux, 1986) and using $\mathcal{O}(2,8)$ order. To minimize the energy reflecting from the boundaries of the model, a perfectly matched layer is used around the model (Berenger, 1994). A single shot of the modeled data is shown in Figure 3a (the baseline data), Figure 3b (the monitor data with perfect repeatability), Figure 3c (the monitor data with NR), and Figure 3d (the noisy monitor data with perfect repeatability). The residuals between the baseline data and the initial data (acquired from the initial model), clean data with perfect repeatability, clean data with NR, and noisy data with perfect repeatability (amplified by a factor of seven) are shown in Figure 3e–3h, respectively. Comparing Figure 3f and Figure 3h shows that the added noise can mask the time-lapse events in the observed data. Figure 3g also shows that the first arrivals can be considered as a time-lapse event in the presence of seawater velocity variation.

In the next section, we discuss the results of the different time-lapse strategies applied to clean and noisy data (S/N = 7) for a perfectly repeated monitor model as well as clean data obtained in the presence of NR. FWI in this study is performed using the PyFWI package (Mardan et al., 2022) which implemented the FWI in the time domain with graphics processing unit programming using OpenCL (Fabien-Ouellet et al., 2017a). Because the initial model (Figure 2d) is rather smooth, cycle skipping is an issue and a multiscale inversion strategy (Bunks et al., 1995) is used with the frequencies of 10, 20,
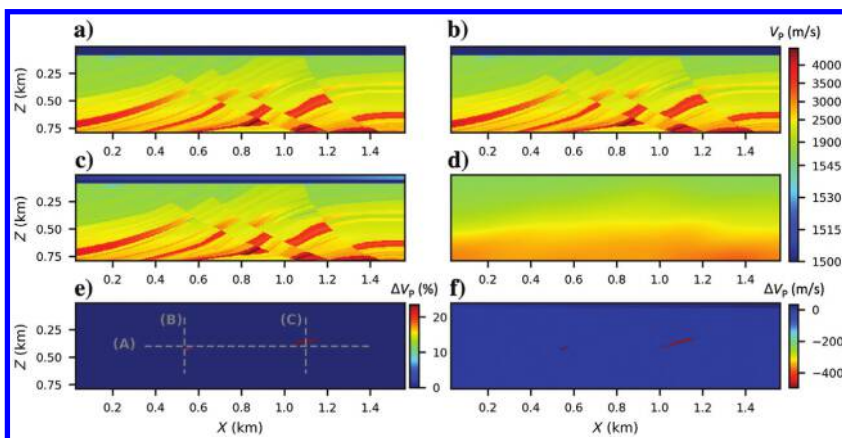

Figure 2. The Marmousi model is used to study the efficiency of different strategies. (a) Baseline, (b) perfectly repeated monitor P-wave velocity model, and (c) monitor model with considering the NR. (d) The smoothed initial model. (e) The absolute value of percent changes between the baseline and monitor model for perfectly repeated model and (f) the true difference between the baseline and monitor model with NR. The gray lines show the location of acquired 1D data used for accuracy analysis in the next section. The specific color scale is used in (a–d) for better visualization of the shallow warm water (NR).

25, 35, and 40 Hz. To minimize the cost functions, we adopted the *l*-BFGS method with 10 iterations for each frequency. As a preconditioner for the inverse Hessian approximation, we scale the gradient by the energy of the forward wavefield (Zhong et al., 2017).

The estimated baseline and monitor models from clean data with perfect repeatability are shown in Figure 4a and 4b, respectively. Although the effects of noise in the data and NR can be hardly visualized in the estimated monitor models (Figure 4c and 4d), the presence of noise in the data and NR can decrease the accuracy of the time-lapse images drastically which is discussed in the next section.

In Figure 5, residuals between the observed data (Figure 3a–3c) and the data obtained by the estimated models (Figure 4) are presented. The residuals are amplified by a factor of seven for better visualization. Figure 5a, 5b, and 5d is obtained by subtracting the "observed data" and estimated data of the clean baseline, clean perfectly repeated monitor, and monitor model with NR, respectively. Figure 5c shows the residuals between the estimated baseline data from the inversion of the noisy data (Figure 3d) and observed clean baseline data (Figure 3a). Figure 5a–5c shows that FWI has been able to recover the subsurface properly. However, the direct waves are not fit perfectly in the monitor model with NR (Figure 5d).

TL-FWI results

In this section, we first assess the performance of the WA inversion. We then compare the performance of all the aforementioned strategies. To compare the results quantitatively, the misfit value,

$$\text{discrepancy} = \frac{(\Delta\mathbf{m}_{\text{true}} - \Delta\mathbf{m}_{\text{est}})^T(\Delta\mathbf{m}_{\text{true}} - \Delta\mathbf{m}_{\text{est}})}{\Delta\mathbf{m}_{\text{true}}^T\Delta\mathbf{m}_{\text{true}}}, \quad (10)$$

is used to present the normalized error in the estimated time-lapse model, where T is the transpose operator, $\Delta\mathbf{m}_{\text{true}}$ is the true difference of the models, and $\Delta\mathbf{m}_{\text{est}}$ is the estimated changes.

WA inversion

The estimated reverse and forward bootstraps for the WA method are shown in Figure 6. As shown by the solid arrows, the artifacts tend to have different signs in different bootstraps which is not the case for the true 4D anomalies (the dashed arrows). Thus, by summing the bootstraps, the artifacts tend to cancel out, whereas the time-lapse changes add up. This property is shown in Figure 7 in which the summation of two bootstraps and their difference is presented for the case of without and with NR. Figure 7a and 7b shows that the averaging can improve the result by better highlighting the true anomalies as shown by the dashed arrows and decreasing the artifacts from the result as shown by the solid arrows. Furthermore, the difference between the two bootstraps provides valuable information on artifacts. This image can show the locations which are most affected by artifacts. To further reduce the artifacts, we propose using the WA method (equation 10). Figure 8 shows the result of WA TL-FWI for different values of β,

ranging from $\beta = 0.2$ to $\beta = 1$ with a step of 0.2. Figure 8 is obtained by analyzing the perfectly repeated monitor model. Variations smaller than 5% of the maximum change are masked out to highlight the effects of β. The true 4D model is shown in Figure 8f. As shown in Figure 8, by adjusting β, the artifacts can be counterbalanced without changing the true anomalies significantly.

Figures 9 and 10 are equivalent to Figure 8 for inversion with noise and NR problem, respectively. As can be noticed, changing the β cannot remove completely the artifacts at the interface of two sublayers of seawater and at the seabed.

WA TL-FWI and its two bootstraps also can be used to have a range of possible time-lapse results (Figure 11). This range is shown as the shaded area in Figure 11 limited between reverse (the red line) and forward (the blue line) bootstraps. The estimated values from other strategies beyond this range should be analyzed skeptically.

To choose an appropriate value for β, the norm of the time-lapse changes is computed as a function of β. We pick the β value that leads to the smallest norm of the time-lapse estimates. Assuming that time-lapse changes are localized, we use the ℓ_1-norm which promotes sparsity and is robust to outliers. Figure 12 shows the ℓ_1-norm of the estimated time-lapse image with different values of β for clean data with perfect repeatability (Figure 12a), noisy data (Figure 12b), and clean data with NR issue (Figure 12c). Considering that the amplitudes of artifacts tend to be depth dependent, we can improve the accuracy by using a depth-dependent β. To do so, we compute the ℓ_1-norm for different depth windows and pick β for each window. In Figure 12, the ℓ_1-norm is used to choose a unique value of β for each depth sample. The solid line in Figure 12 shows the optimal value of β that can maximize the match between the result of the WA method and the true time-lapse changes, whereas
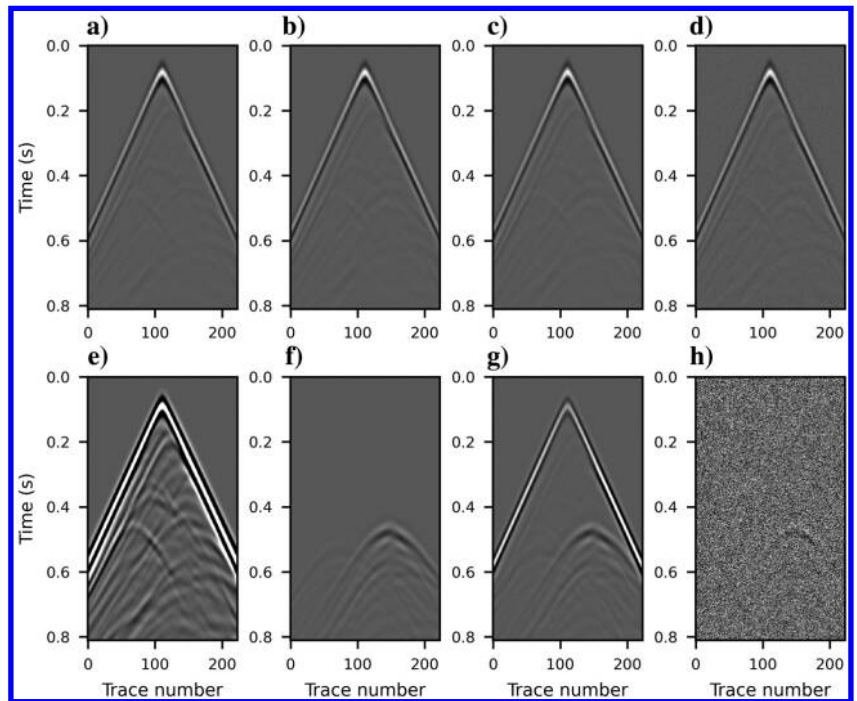

Figure 3. The observed data from (a) baseline, (b) monitor model with perfect repeatability, (c) monitor model with NR, and (d) monitor model with noise. Difference of the baseline data with (e) initial data, (f) monitor data with perfect repeatability, (g) monitor data with NR, and (h) monitor data with noise. All residuals (e–h) are amplified by a factor of seven for better visualization.

the dashed line shows the estimated β using ℓ_1-norm. As can be seen, the β chosen as the minimum ℓ_1-norm reproduces very well the optimal value. The root-mean-square (rms) error between the estimated and best β is shown in Figure 12 for all cases, which show a very good fit. As the optimal value is unknown in a real case, the ℓ_1-norm criteria can be chosen as a good proxy.

Having a time-lapse anomaly at a depth window, the ℓ_1-norm increases because this norm measures the absolute value of time-lapse changes and artifacts. Thereby, time-lapse anomalies in the model can be detected using the increase of ℓ_1-norm in Figure 12 around the depth of 0.4 km. Note that the NR in the seawater velocity causes strong artifacts in the model that can be seen as the extreme value of ℓ_1-norm in Figure 12c.

Comparison of time-lapse strategies

We compared all discussed time-lapse strategies on two different aspects, computation cost and discrepancy (equation 10). The computation time and the discrepancy of each strategy are provided in Table 1. The number of required FWI and or joint TL-FWI for performing each method is presented in the first column. As the cascaded method is the fastest method among the studied strategies, the computation time of every method is presented with respect to the computation time of the cascaded method in the second column.

Figures 13, 14, and 15 show the results of the TL-FWI obtained with all presented strategies. The poor accuracy of the cascaded method is shown in Figures 13a–15a. This method produces strong artifacts. The results of the CU method (Figures 13b–15b) appear to be better than the ones of the cascaded method but still contain noticeable amounts of artifacts. Figures 13c–15c show the results of the CD method. Although this method can suppress the artifacts in clean data, it has difficulties to deal with noisy data. From a qualitative point of view, the results of the WA inversion (Figures 13d–15d) and simultaneous TL-FWI (Figures 13e–15e) seem better interpretable. This is supported by analyzing Table 1 and

the quantitative study of the accuracy of the estimated time-lapse changes. Note that the value of β with minimum of ℓ_1-norm (the dashed lines in Figure 12) is used to obtain the results of the WA method shown in Figures 13d–15d.

As can be expected after a comparison of the results (Figures 13–15), the error of the CC is higher than the one of the other strategies. The WA method requires three FWI runs (one less than the CU and CD methods) and provides the most accurate result of all strategies. From Table 1, we can notice that SI is the third fastest strategy and provides good accuracy. However, the accuracy and computation time of this method depend on the choice of the regularization parameter (equation 9). Hence, although the joint inversion can address a variety of artifacts, choosing an appropriate regularization parameter is a tedious task.

Misfit analysis of the results

The results of the different methods along the three lines (shown in the dashed gray in Figure 2e) are analyzed in Figure 16. Figure 16a–16c shows the estimated time lapse with perfect repeatability and Figure 16d–16f is obtained by considering NR.
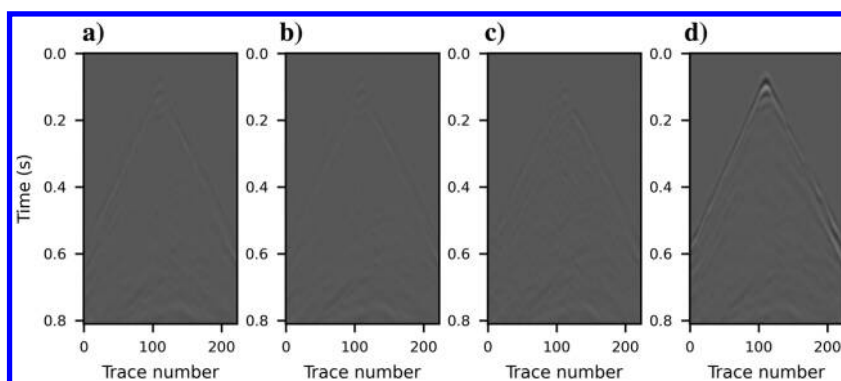

Figure 5. Residuals between the estimated data and true data (Figure 3a–3c) in the case of (a) baseline data, (b) clean monitor data with perfect repeatability, (c) noisy monitor data with perfect repeatability, and (d) clean monitor data with NR. All residuals are amplified by a factor of seven for better visualization.
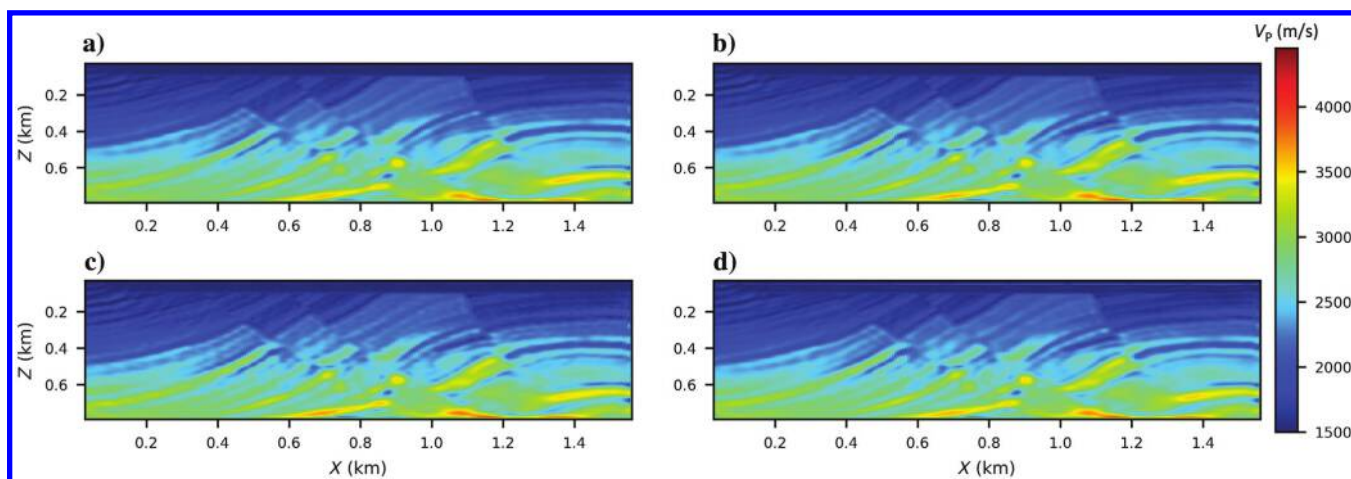

Figure 4. The result of FWI from inverting (a) baseline data, (b) clean monitor data with perfect repeatability, (c) noisy monitor data with perfect repeatability, and (d) clean monitor data with NR.

As shown by the green arrows in Figure 16a–16c, the CU method is prone to generate spurious events more than all other strategies. Figure 16 shows that there is a good consistency among CD, WA, and SI. Note that the result of the cascaded method is not presented here as we already showed that this method does not provide an accurate time-lapse estimate.

Generalization with SEAM data

To confirm the previous analysis, we applied WA TL-FWI to the SEAM synthetic seismic data. In 2016, a collaborative project of SEG and SPE created a pilot project to study the efficiency of geophysical remote sensing to quantify the changes in oil and gas reservoirs inspired by a geologic model of the Gulf of Mexico (Oppert et al., 2017). The coupled three-phase fluid flow and geomechanical response are simulated by considering 11 production and six water-injection wells. These wells are used to simulate 27.5 months of daily production at a simulated rate of 67,500 barrels and water injection of 32,500 barrels.

Although this model represents an area of $12.5 \text{ km}^2 \times 12.5 \text{ km}^2$ with a 5 km depth, in this study, we focused on a smaller part. A 2D plane of this model from a depth of 2.6 to 4.8 km is studied. The baseline and monitor models in the studied region are shown

Table 1. Computation time and discrepancy for different strategies: CC, CU, CD, WA, and SI.

	Computation time		Discrepancy		
	FWI runs	With respect to CC	Clean data	Noisy data	With NR
CC	2	**1**	3.301	3.381	5.047
CU	4	1.871	0.915	1.659	2.080
CD	4	1.860	0.819	1.368	2.163
WA	3	1.480	**0.734**	**1.098**	**1.835**
SI	1 + 1 joint TL-FWI	1.517	0.756	1.216	1.969
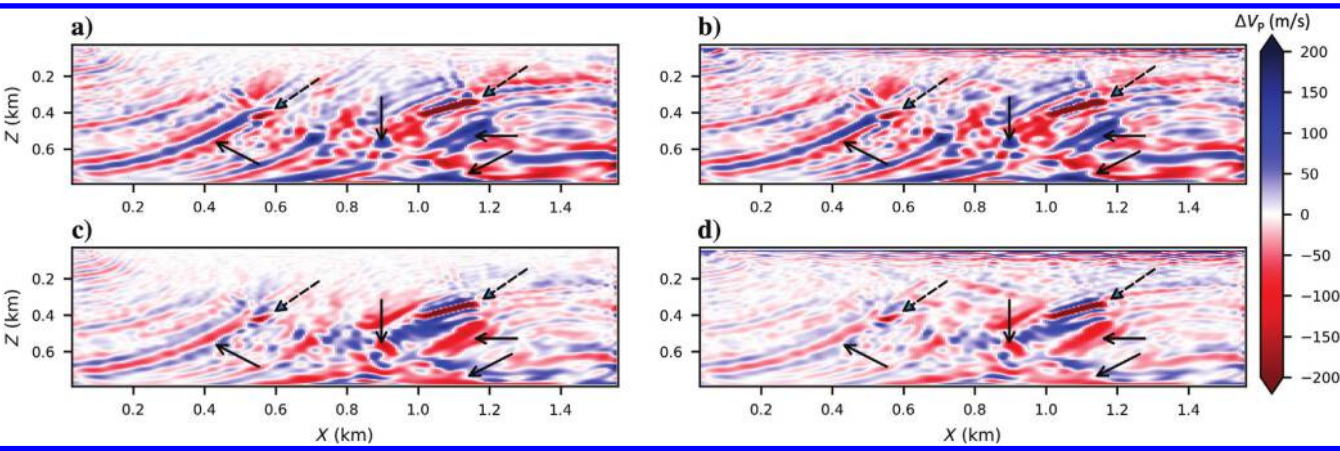
Figure 6. (a and b) Reverse and (c and d) forward bootstraps with a symmetric color scale. (a and c) The bootstraps obtained from the data with perfect repeatability and (b and d) the bootstraps in the presence of NR. Solid arrows point to the artifacts and dashed arrows point to the sought anomalies.
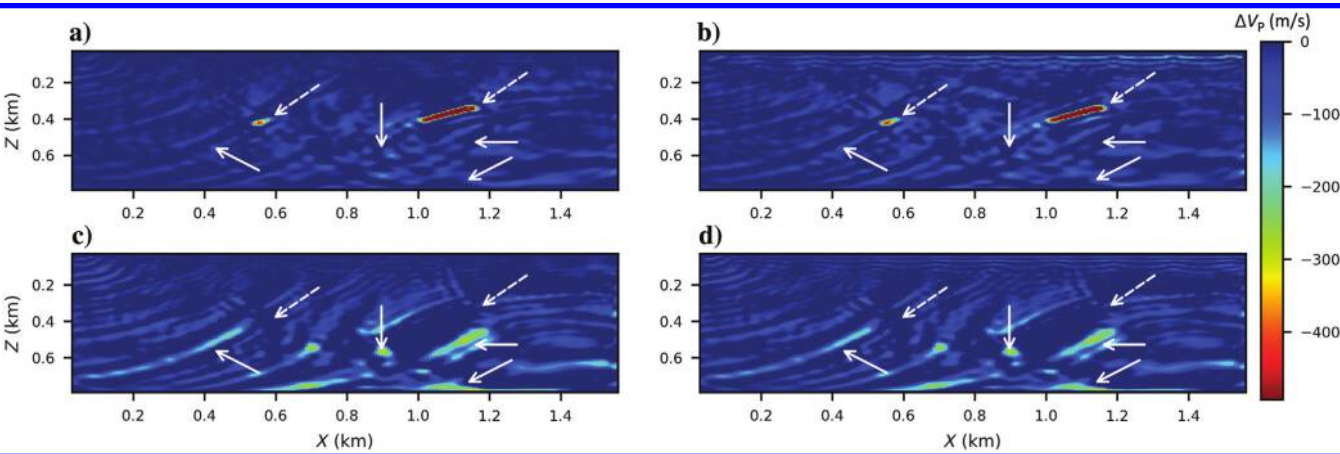

Figure 7. (a and b) Summation of the reverse and forward bootstraps. (c and d) Difference between reverse and forward bootstraps. (a and c) Obtained from the data with perfect repeatability and (b and d) estimated in the presence of NR. Solid arrows point to the artifacts and dashed arrows point to the sought anomalies.

in Figure 17a and 17b, respectively. As shown with the dashed lines, this zone consists of three normal faults. The turbidite reservoir which starts at approximately 3.3 km can be characterized by lower P-wave velocity due to the presence of gas. P-wave velocity then gradually increases below the gas-oil contact (GOC) due to the presence of oil and then water. The injection to and production from the reservoir affected different parts of the model differently. Fluid substitution (oil replacing gas) and reservoir compaction increased the P-wave velocity significantly in the original gas cap. However, velocity decreases in the aquifer below the oil-water contact (OWC) because of water injection and reservoir depletion. The true time-lapse image is shown in Figure 17c.
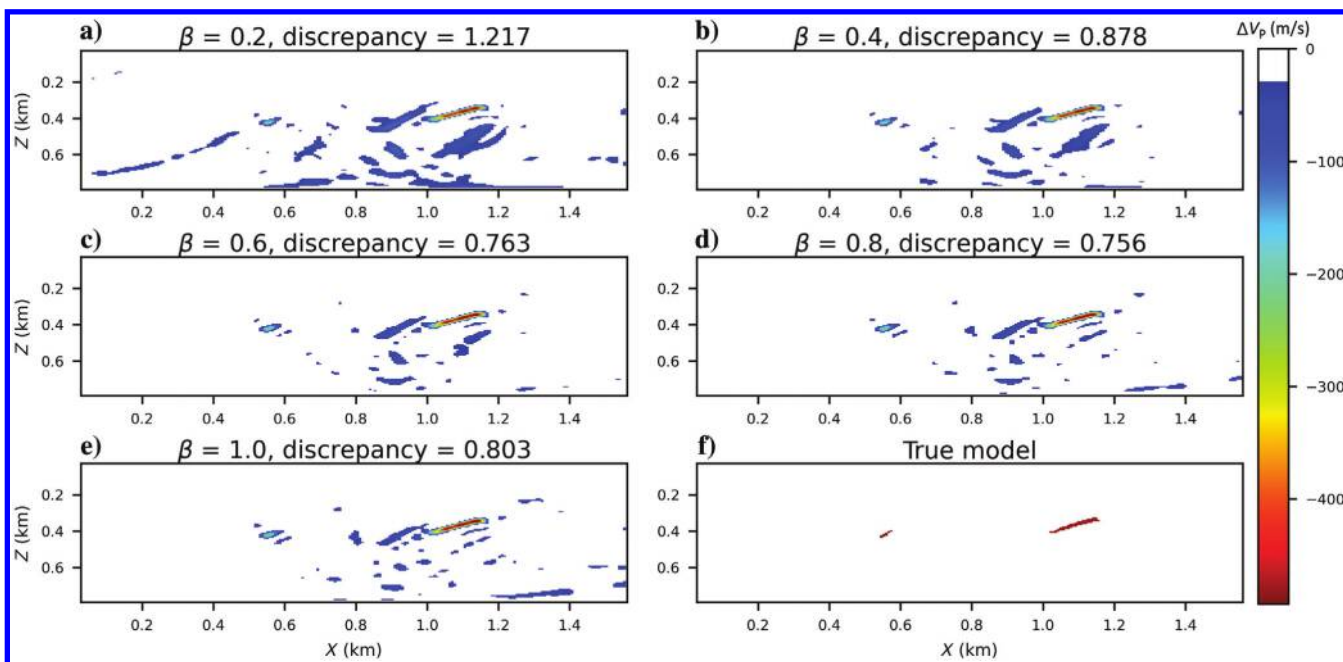
Figure 8. Results of the WA method with different values of β with perfect repeatability: (a) $\beta = 0.2$, (b) $\beta = 0.4$, (c) $\beta = 0.6$, (d) $\beta = 0.8$, and (e) $\beta = 1.0$. The optimum value of β for this model is 0.8 with an error of 0.756. (f) True time-lapse changes. For better visualization, the changes less than 5% of maximum change are masked out.
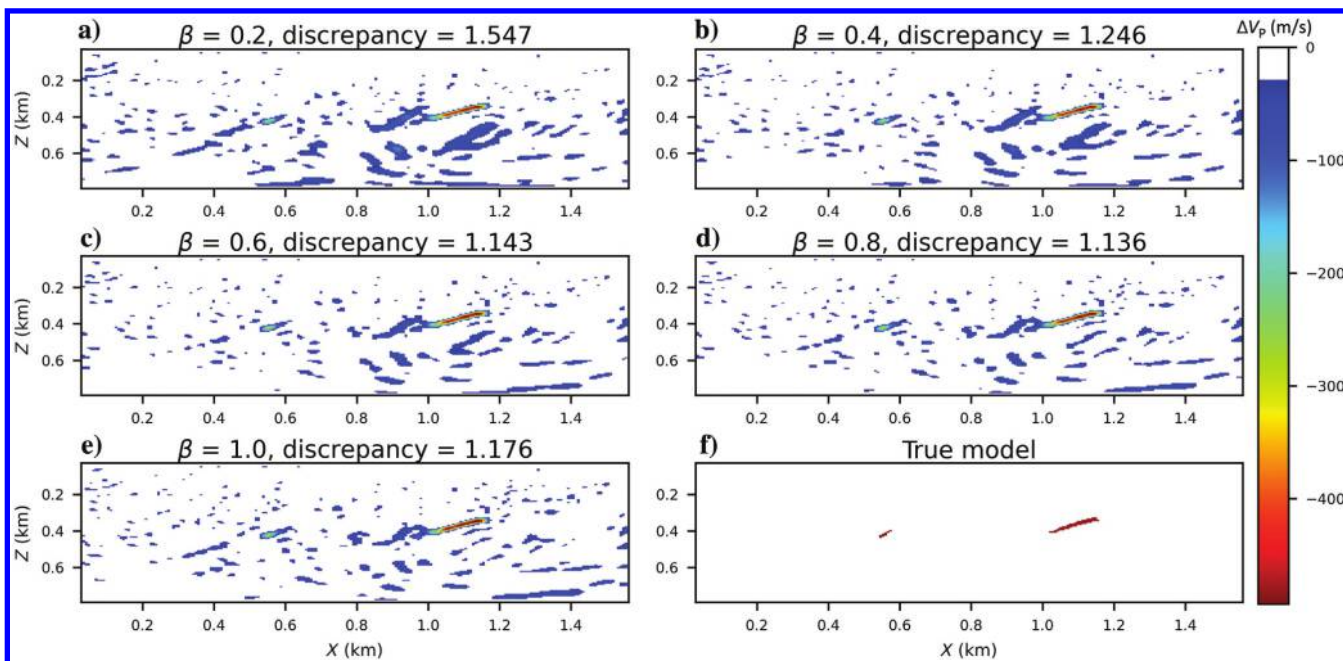
Figure 9. Results of the WA method with different values of β by using noisy data: (a) $\beta = 0.2$, (b) $\beta = 0.4$, (c) $\beta = 0.6$, (d) $\beta = 0.8$, and (e) $\beta = 1.0$. The optimum value of β for noisy data is 0.8 with an error of 1.136. (f) True time-lapse changes. For better visualization, the changes less than 5% of maximum change are masked out.
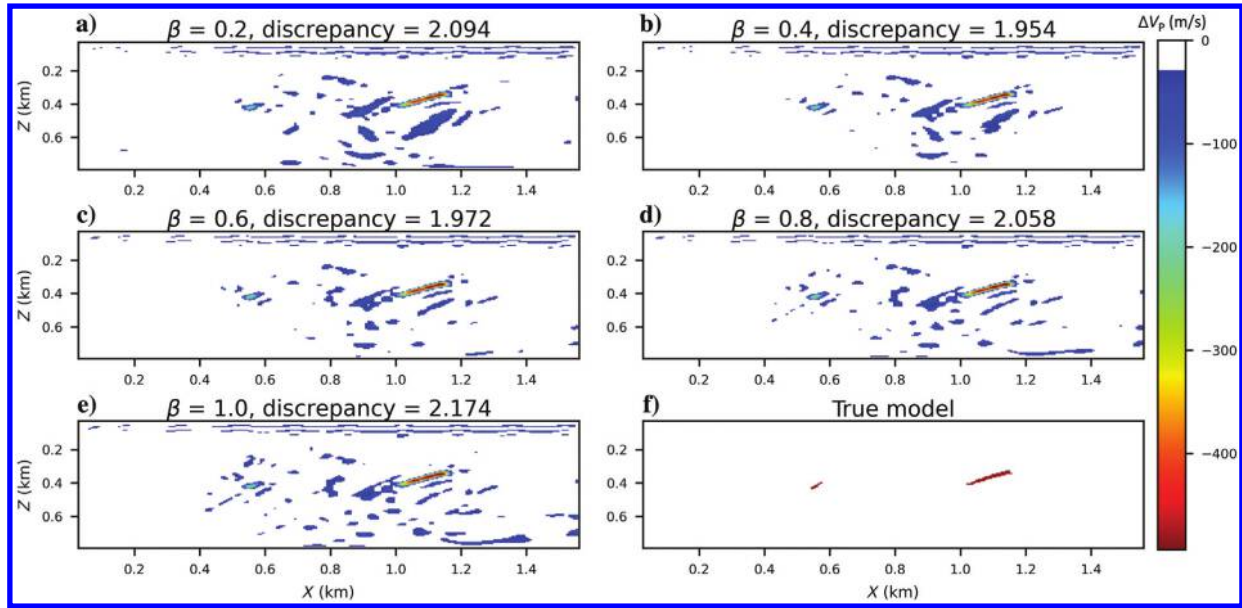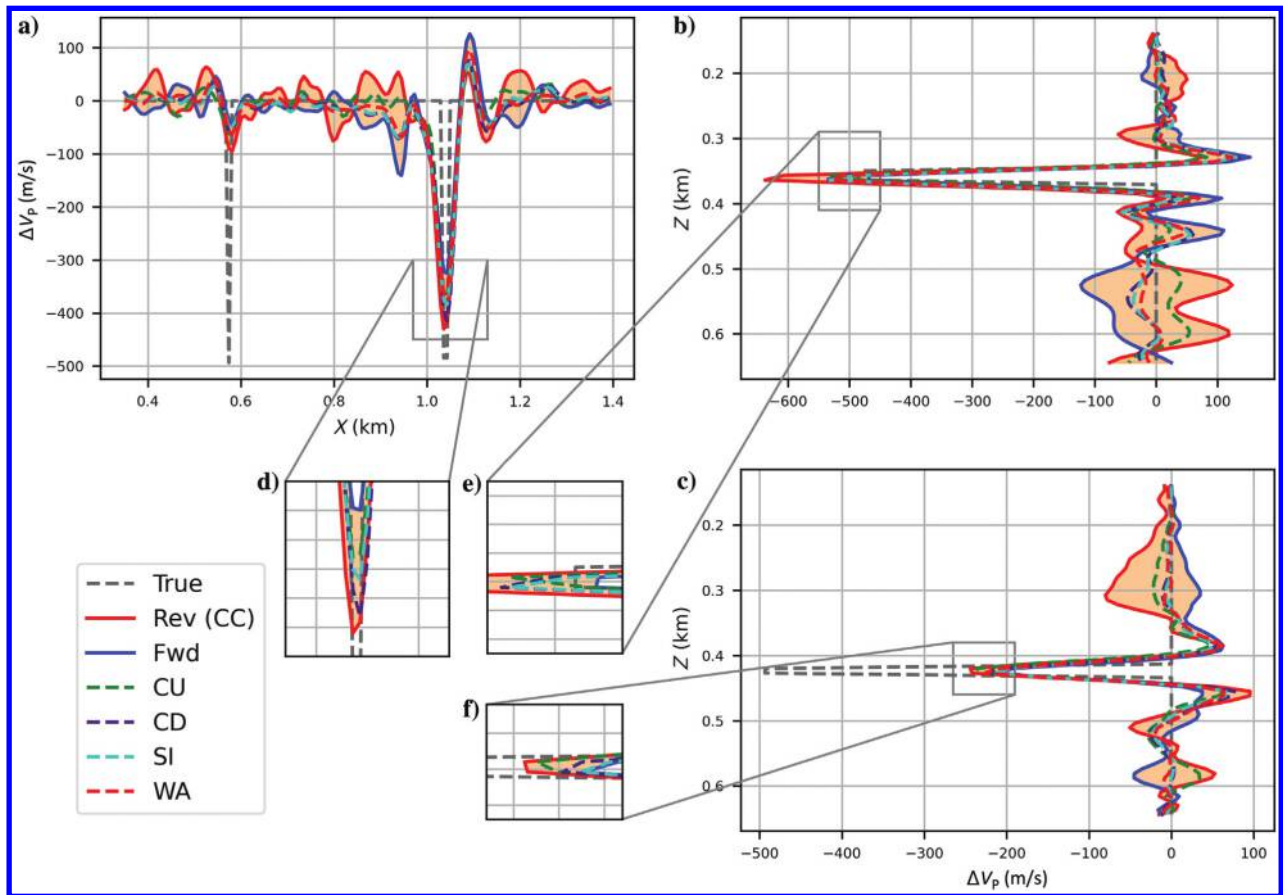
Figure 10. Results of the WA method with different values of β with NR: (a) $\beta = 0.2$, (b) $\beta = 0.4$, (c) $\beta = 0.6$, (d) $\beta = 0.8$, and (e) $\beta = 1.0$. The optimum value of β for noiseless data is 0.4 with an error of 1.954. (f) True time-lapse changes. For better visualization, the changes less than 5% of maximum change are masked out.

Figure 11. The WA TL-FWI can provide a range (the shaded area) for possible time-lapse results from other methods. This range is limited between the reverse (the red line) and forward (the blue line) bootstraps. The location of (a–c) is shown in Figure 2e.
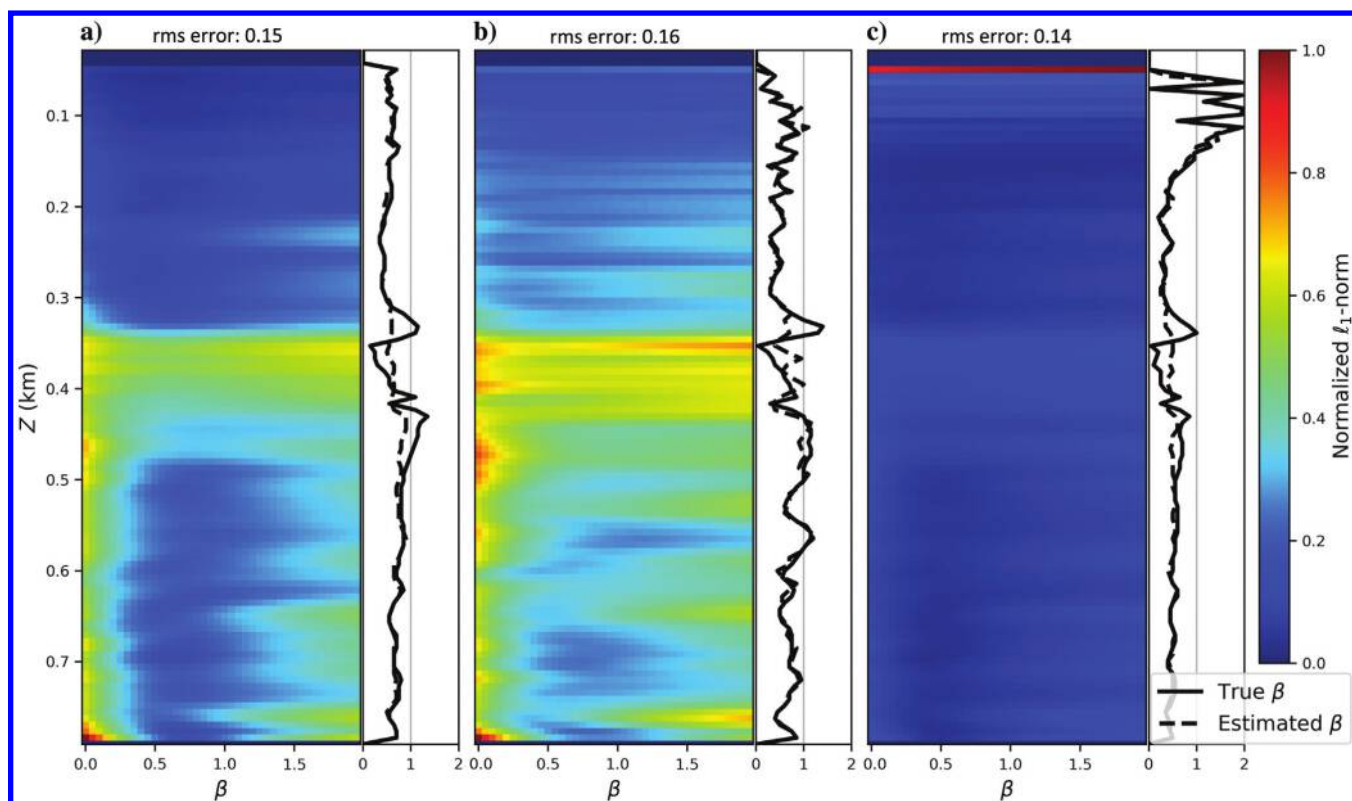
Figure 12. The ℓ_1-norm of the estimated time-lapse image can be plotted versus different values of β to obtain an insight into the optimum value of β for the WA method. This technique is used with a window size of one sample for TL-FWI of (a) clean data with perfect repeatability, (b) noisy data with perfect repeatability, and (c) clean data with NR. The 1D plots show the best value of β in the solid line and the estimated β using ℓ_1-norm in the dashed line.
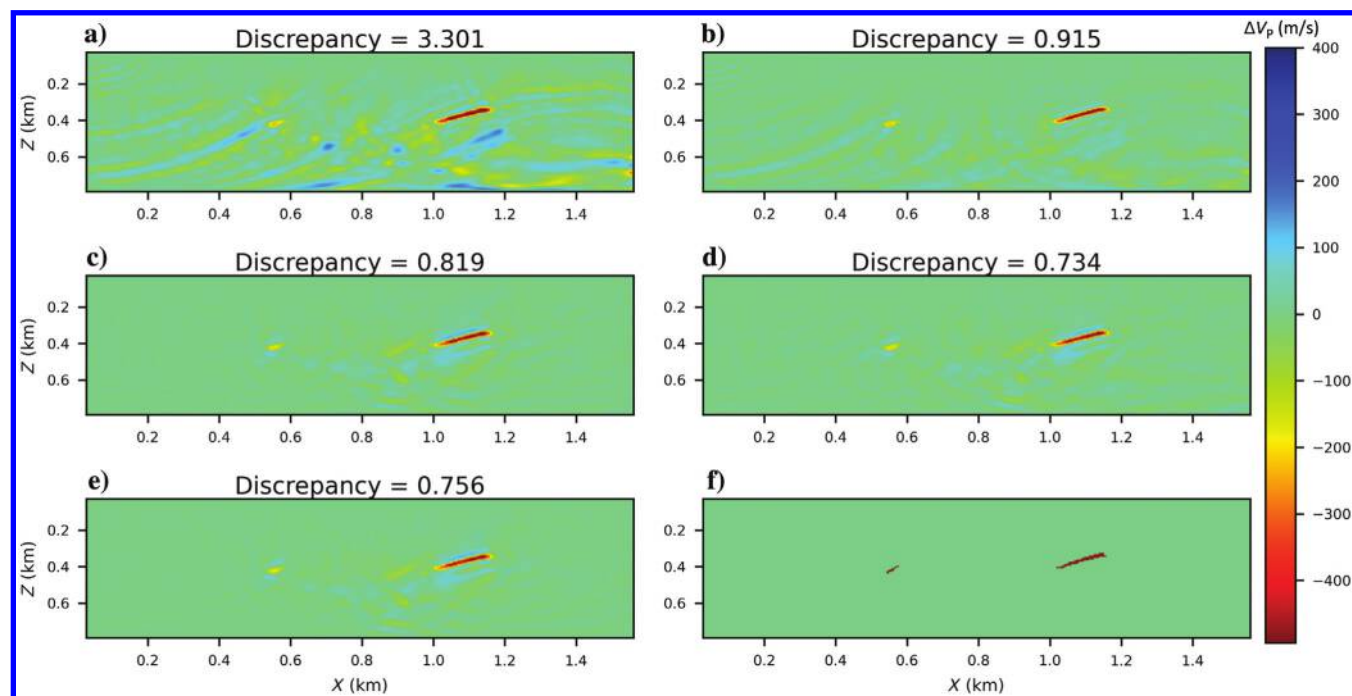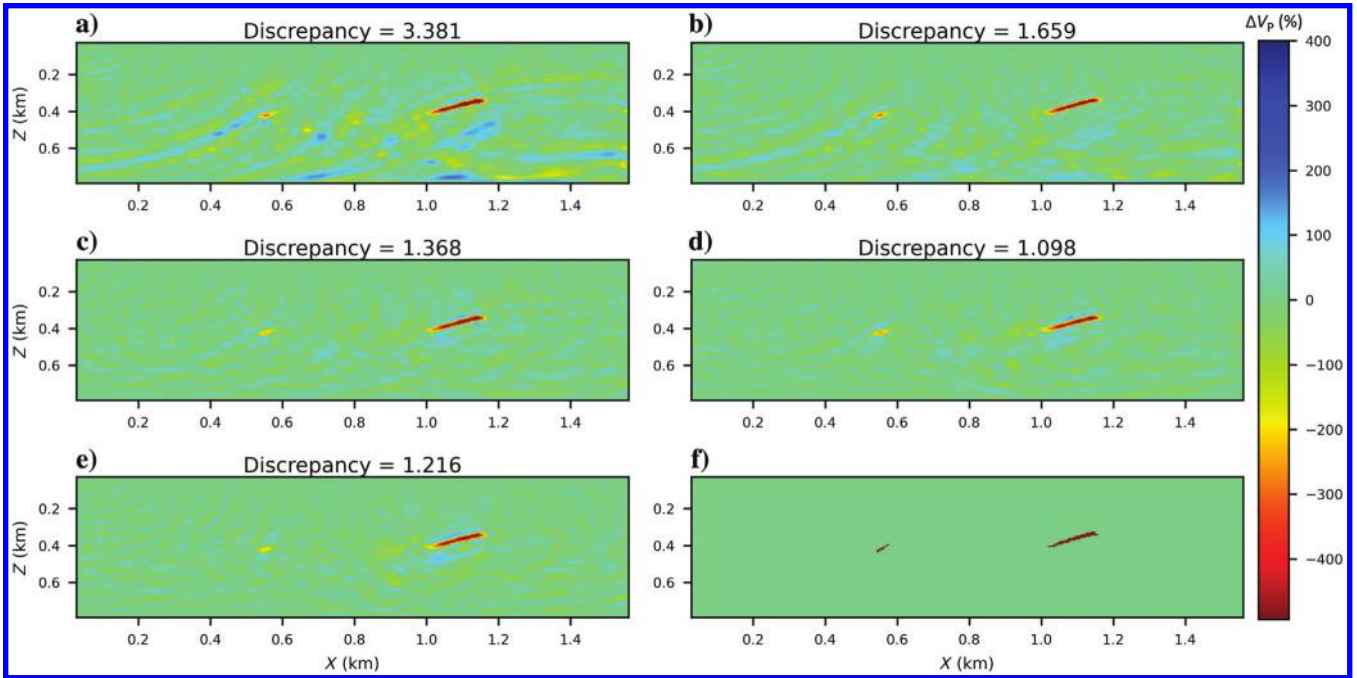

Figure 13. Results of different methods using clean data with perfect repeatability. (a) CC, (b) CU, (c) CD, (d) WA, (e) simultaneous TL-FWI, and (f) true time-lapse model.

To assess the efficiency of the WA TL-FWI, the surface acquisition is carried out by using the sources at the depth of 10 m and at a regular interval of 25 m. The sources propagate the Ricker wavelet with a central frequency of 25 Hz. We use the multiscale inversion strategy with frequencies of 10, 15, 20, 25, 30, 35, and 70 Hz. The

estimated time-lapse image is shown in Figure 17d for WA inversion. The estimated changes accurately reproduce the large-scale changes in the reservoir. The changes in the gas layer at the top of the reservoir also are well recovered. The OWC and GOC are marked by points at the beginning and the end. The WA method

Figure 14. Results of different methods using noisy data with perfect repeatability. (a) CC, (b) CU, (c) CD, (d) WA, (e) simultaneous TL-FWI, and (f) true time-lapse model.
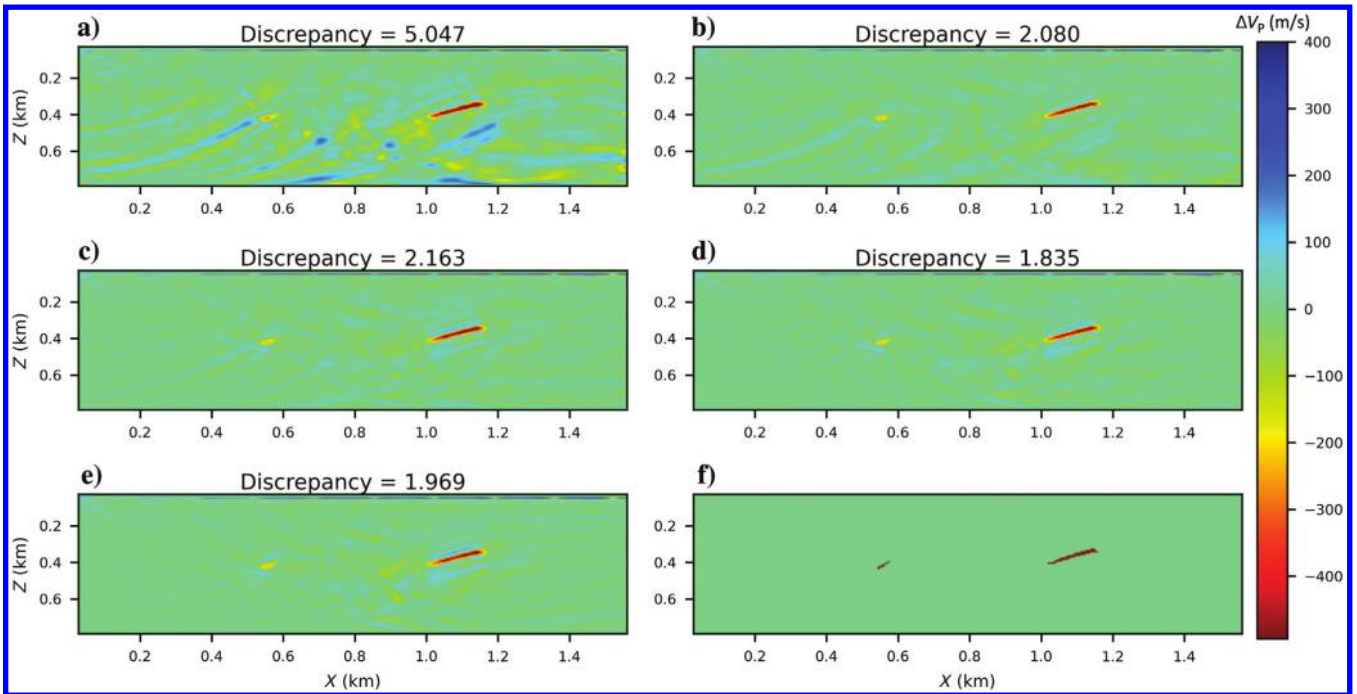
Figure 15. Results of different methods using clean data with NR. (a) CC, (b) CU, (c) CD, (d) WA, (e) simultaneous TL-FWI, and (f) true time-lapse model.
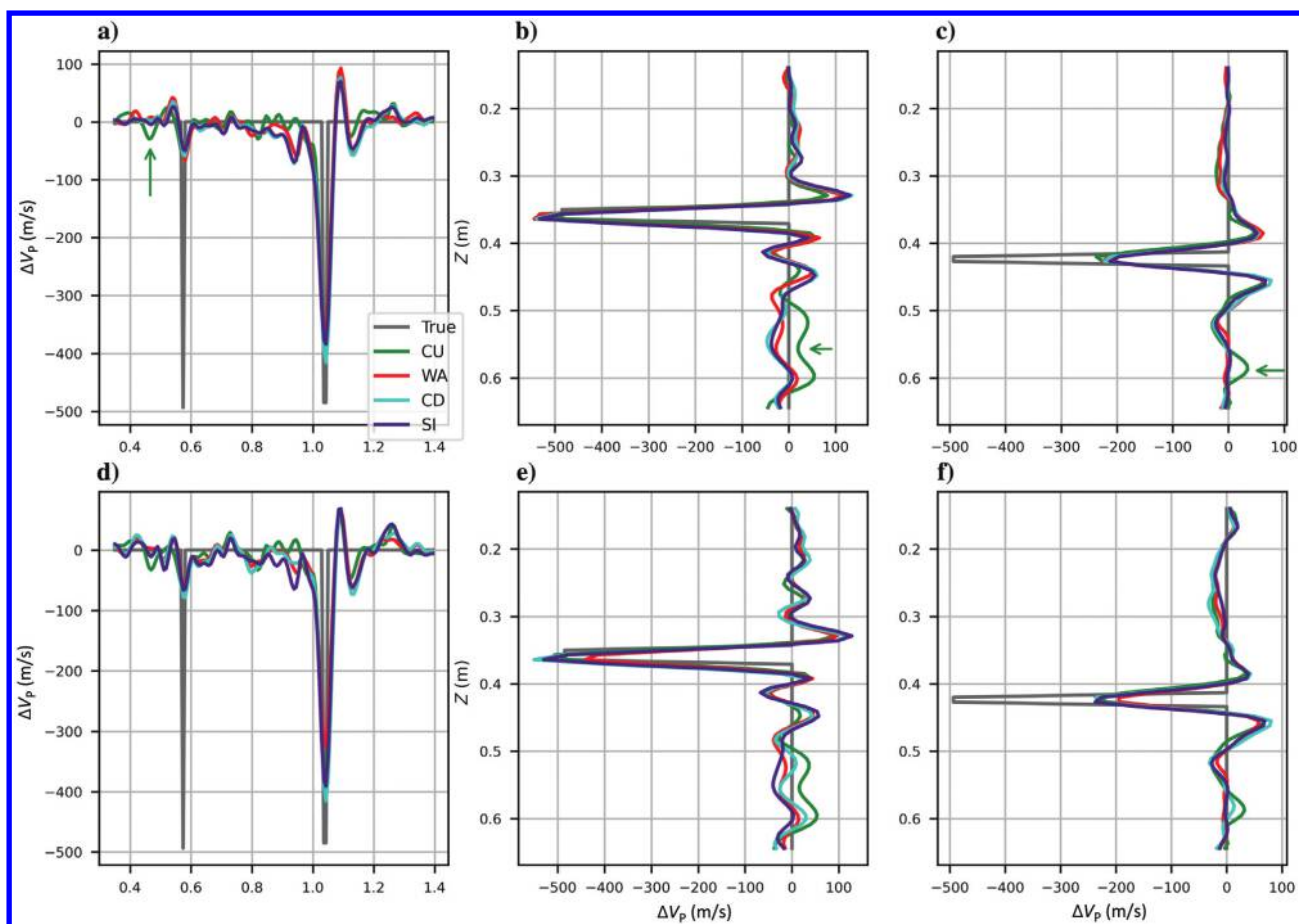
Figure 16. The 1D presentation of the estimated model for inversion of clean data from (a–c) perfectly repeated monitor model and (d–f) monitor model with NR. The location of the data is shown in Figure 2e. (a and d) Acquired along line **A**, (b and e) obtained vertically at $x = 553$ m by line **B**, and (c and f) at $x = 1106$ m along line **C**. Green arrows show the inconsistency of the result of the CU method, whereas other methods provide very coherent estimates.

Figure 17. The SEAM model is used to verify the accuracy of the WA method. (a) The baseline and (b) monitor models. (c) The true time-lapse image and (d) the estimated time-lapse changes of the SEAM model by the WA method.
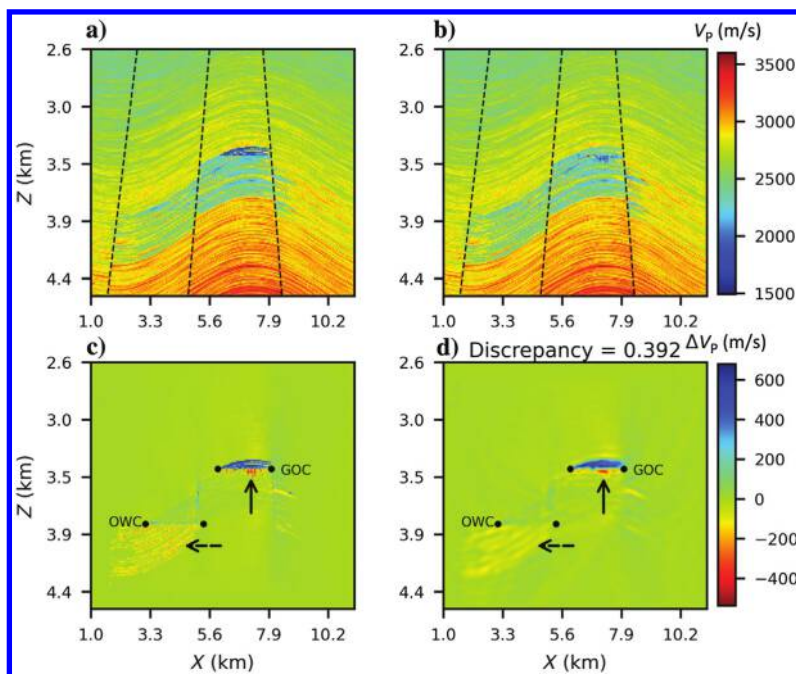
also has been able to delineate the changes beneath the GOC (the solid arrow). Finally, the changes in the aquifer are recovered very well. The lack of resolution prevented the TL-FWI algorithm to image accurately the sharp changes at the OWC and beneath it as shown by the dashed arrow.

It should be mentioned that the time-lapse changes in both analyzed models have a strong magnitude. Although the results show that the WA method provides the highest accuracy with acceptable computation time, weaker time-lapse anomalies can challenge all discussed methods at different levels. Hence, the potential of these methods should be analyzed further by assessing their efficiency for recovering different magnitudes of time-lapse anomalies.

CONCLUSION

Time-lapse imaging using seismic data is a crucial field of study that can be used in the oil industry (production/injection) and CO_2 storage. Due to the fact that the time-dependent changes in each of these applications are very small with respect to the prior state, time-lapse FWI is more difficult than just implementing two independent FWI and taking their difference. Therefore, we presented the WA method and compared it against the cascaded inversion, CU, CD, and SI methods. Comparisons of the methods on two benchmark models showed that the WA method leads to the most accurate time-lapse estimates while it is one of the fastest approaches. Furthermore, WA inversion allows for the reduction of the presence of artifacts and points to uncertain features in the model. Having two time-lapse estimates at the end of TL-FWI, different criteria can be used to select the weight for the WA method. As shown in this study, ℓ_1-norm can be used to find an appropriate value for this parameter. The simultaneous TL-FWI can provide comparable performance (accuracy and computation time) with the disadvantage of requiring a regularization parameter which can change the accuracy and the computation time significantly.

ACKNOWLEDGMENTS

DATA AND MATERIALS AVAILABILITY

Data associated with this research are available and can be obtained by contacting the corresponding author.

REFERENCES

Altan, S., 1997, Time-lapse seismic monitoring: Repeatability processing tests: 67th Annual International Meeting, SEG, Expanded Abstracts, 866–867, doi: 10.1190/1.1886151.
Asnaashari, A., R. Brossier, S. Garambois, F. Audebert, P. Thore, and J. Virieux, 2015, Time-lapse seismic imaging using regularized full-waveform inversion with a prior model: Which strategy?: Geophysical Prospecting, **63**, 78–98, doi: 10.1111/1365-2478.12176.
Berenger, J.-P., 1994, A perfectly matched layer for the absorption of electromagnetic waves: Journal of Computational Physics, **114**, 185–200, doi: 10.1006/jcph.1994.1159.
Biondi, B., G. Mavko, T. Mukerji, J. Rickett, D. Lumley, C. Deutsch, R. Gundes, and M. Thiele, 1998, Reservoir monitoring: A multidisciplinary feasibility study: The Leading Edge, **17**, 1404–1414, doi: 10.1190/1.1437860.

Bunks, C., F. M. Saleck, S. Zaleski, and G. Chavent, 1995, Multiscale seismic waveform inversion: Geophysics, **60**, 1457–1473, doi: 10.1190/1.1443880.
Davis, K., Y. Li, and M. Batzle, 2008, Time-lapse gravity monitoring: A systematic 4D approach with application to aquifer storage and recovery: Geophysics, **73**, no. 6, WA61–WA69, doi: 10.1190/1.2987376.
Fabien-Ouellet, G., E. Gloaguen, and B. Giroux, 2017a, Time-domain seismic modeling in viscoelastic media for full waveform inversion on heterogeneous computing platforms with OpenCL: Computers & Geosciences, **100**, 142–155, doi: 10.1016/j.cageo.2016.12.004.
Fabien-Ouellet, G., E. Gloaguen, and B. Giroux, 2017b, Time domain viscoelastic full waveform inversion: Geophysical Journal International, **209**, 1718–1734, doi: 10.1093/gji/ggx110.
Giertzuch, P.-L., J. Doetsch, M. Jalali, A. Shakas, C. Schmelzbach, and H. Maurer, 2020, Time-lapse ground penetrating radar difference reflection imaging of saline tracer flow in fractured rock: Geophysics, **85**, no. 3, H25–H37, doi: 10.1190/geo2019-0481.1.
Hayley, K., A. Pidlisecky, and L. R. Bentley, 2011, Simultaneous time-lapse electrical resistivity inversion: Journal of Applied Geophysics, **75**, 401–411, doi: 10.1016/j.jappgeo.2011.06.035.
Hicks, E., H. Hoeber, M. Houbiers, S. P. Lescoffit, A. Ratcliffe, and V. Vinje, 2016, Time-lapse full-waveform inversion as a reservoir-monitoring tool — A North Sea case study: The Leading Edge, **35**, 850–858, doi: 10.1190/tle35100850.1.
Kamei, R., and D. Lumley, 2017, Full waveform inversion of repeating seismic events to estimate time-lapse velocity changes: Geophysical Journal International, **209**, 1239–1264, doi: 10.1093/gji/ggx057.
Li, Y., T. Alkhalifah, and Q. Guo, 2021, Target-oriented time-lapse waveform inversion using deep learning-assisted regularization: Geophysics, **86**, no. 4, R485–R495, doi: 10.1190/geo2020-0383.1.
Lumley, D. E., 1995a, 4-D seismic monitoring of an active steamflood: 65th Annual International Meeting, SEG, Expanded Abstracts, 203–206, doi: 10.1190/1.1887497.
Lumley, D. E., 1995b, Seismic time-lapse monitoring of subsurface fluid flow: Ph.D. thesis, Stanford University.
Maharramov, M., and B. Biondi, 2014, Robust joint full-waveform inversion of time-lapse seismic data sets with total-variation regularization: arXiv: Geophysics.
Maharramov, M., B. L. Biondi, and M. A. Meadows, 2016, Time-lapse inverse theory with applications: Geophysics, **81**, no. 6, R485–R501, doi: 10.1190/geo2016-0131.1.
Mardan, A., B. Giroux, and G. Fabien-Ouellet, 2022, PyFWI: Python package for full-waveform inversion (FWI): Zenodo, doi: 10.5281/zenodo.5813637.
Nocedal, J., and S. J. Wright, 2006, Numerical optimization: Springer.
Oppert, S., J. Stefani, D. Eakin, A. Halpert, J. V. Herwanger, A. Bottrill, P. Popov, L. Tan, V. Artus, and M. Oristaglio, 2017, Virtual time-lapse seismic monitoring using fully coupled flow and geomechanical simulations: The Leading Edge, **36**, 750–768, doi: 10.1190/tle36090750.1.
Plessix, R., S. Michelet, H. Rynja, H. Kuehl, C. Perkins, J. de Maag, and P. Hatchell, 2010, Some 3D applications of full waveform inversion: 72nd Annual International Conference and Exhibition, EAGE, Extended Abstracts, doi: 10.3997/2214-4609.20149933.
Pratt, R. G., and M. H. Worthington, 1990, Inverse theory applied to multisource cross-hole tomography: Geophysical Prospecting, **38**, 287–310, doi: 10.1111/j.1365-2478.1990.tb01846.x.
Raknes, E. B., W. Weibull, and B. Arntsen, 2013, Time-lapse full waveform inversion: Synthetic and real data examples: 83rd Annual International Meeting, SEG, Expanded Abstracts, 944–948, doi: 10.1190/segam2013-0540.1.
Routh, P., G. Palacharla, I. Chikichev, and S. Lazaratos, 2012, Full wavefield inversion of time-lapse data for improved imaging and reservoir characterization: 82nd Annual International Meeting, SEG, Expanded Abstracts, doi: 10.1190/segam2012-1043.1.
Routh, P. S., and P. D. Anno, 2008, Time-lapse noise characterization by inversion: 78th Annual International Meeting, SEG, Expanded Abstracts, 3143–3147, doi: 10.1190/1.3063999.
Tarantola, A., 1984, Inversion of seismic reflection data in the acoustic approximation: Geophysics, **49**, 1259–1266, doi: 10.1190/1.1441754.
Virieux, J., 1986, P-SV wave propagation in heterogeneous media: Velocity-stress finite-difference method: Geophysics, **51**, 889–901, doi: 10.1190/1.1442147.
Virieux, J., A. Asnaashari, R. Brossier, L. Metivier, A. Ribodetti, and W. Zhou, 2017, An introduction to full waveform inversion: SEG.
Virieux, J., and S. Operto, 2009, An overview of full-waveform inversion in exploration geophysics: Geophysics, **74**, no. 6, WCC1–WCC26, doi: 10.1190/1.3238367.
Watanabe, T., S. Shimizu, E. Asakawa, and T. Matsuoka, 2005, Differential waveform tomography for time-lapse crosswell seismic data with application to gas hydrate production monitoring: 75th Annual International Meeting, SEG, Expanded Abstracts, 2323–2326, doi: 10.1190/1.1845221.

Yang, D., F. Liu, S. Morton, A. Malcolm, and M. Fehler, 2016, Time-lapse full-waveform inversion with ocean-bottom-cable data: Application on Valhall field: Geophysics, **81**, no. 4, R225–R235, doi: 10.1190/geo2015-0345.1.

Zhong, M., J. Tan, P. Song, X. Bo Zhang, C. Xie, and Z. Lun Liu, 2017, Time-domain full waveform inversion using the gradient preconditioning based on seismic wave energy: Application to the South China Sea: International Geophysical Conference, 440–443, doi: 10.1190/IGC2017-113.

Zhou, W., and D. Lumley, 2021a, Central-difference time-lapse 4D seismic full-waveform inversion: Geophysics, **86**, no. 2, R161–R172, doi: 10.1190/geo2019-0834.1.

Zhou, W., and D. Lumley, 2021b, Nonrepeatability effects on time-lapse 4D seismic full-waveform inversion for ocean-bottom node data: Geophysics, **86**, no. 4, R547–R561, doi: 10.1190/geo2020-0577.1.

Biographies and photographs of the authors are not available.